Solving microscopic flow problems using Stokes equations in SPH

Paul van Liedekerke, Bart Smeets, Tim Odenthal, Engelbert Tijskens, Herman Ramon

Solving microscopic flow problems using Stokes equations in SPH

P. Van Liedekerke[a,*], B. Smeets[b], T. Odenthal[b], E. Tijskens[b], H. Ramon[b]

[a] *INRIA, Domaine Rocquencourt, B.P. 105, 78153 Le Chesnay Cedex, France*
[b] *BIOSYST-MeBioS, KULeuven, Kasteelpark Arenberg 30, 3001 Leuven, Belgium*

Abstract

Starting from the Smoothed Particle Hydrodynamics method (SPH), we propose an alternative way to solve flow problems at a very low Reynolds number. The method is based on an explicit drop out of the inertial terms in the normal SPH equations, and solves the coupled system to find the velocities of the particles using the conjugate gradient method. The method will be called NSPH which refers to the non-inertial character of the equations. Whereas the time-step in standard SPH formulations for low Reynolds numbers is linearly restricted by the inverse of the viscosity and quadratically by the particle resolution, the stability of the NSPH solution benefits from a higher viscosity and is independent of the particle resolution. Since this method allows for a much higher time-step, it solves creeping flow problems with a high resolution and a long timescale up to three orders of magnitude faster than SPH. In this paper, we compare the accuracy and capabilities of the new NSPH method to canonical SPH solutions considering a number of standard problems in fluid dynamics. In addition, we show that NSPH is capable of modeling more complex physical phenomena such as the motion of a red blood cell in plasma.

Keywords: SPH, Stokes flow, microfluidics, red blood cell

1. Introduction

Life at a microscopic scale is governed by fluid dynamics at a low Reynolds number (Re). If the dynamics is dominated by friction and inertial effects can be neglected, the flow through narrow channels and in small cavities appears to be instantaneous and time-reversible. Typical examples in nature are the swimming of microorganisms and the motion of red blood cells (RBC) in capillaries. A fluid described at these scales also starts to *feel* the fluctuations on the hydrodynamic variables and as a result the hydrodynamics should be treated as *Fluctuating Hydrodynamics* [1]. Thermal fluctuations give rise to diffusional

*Corresponding author
Email address: paul.van_liedekerke@inria.fr (P. Van Liedekerke)

processes, though these processes may be slow compared to the streaming motion of an object. For example, the positional timescale of a RBC as a result of diffusion is much larger than compared to the timescale due to traveling with the plasma flow in the capillary. In problems in which one can ignore the thermal agitation and adopt the $Re \ll 1$ assumption, one typically applies the Stokes equations, a linear and easier-to-solve case of the Navier-Stokes equations (NS):

$$\nabla p - \eta \nabla^2 \boldsymbol{v} = \boldsymbol{F}, \tag{1}$$

In this equation, p is the pressure, η is the viscosity, and $\boldsymbol{v}$ is the velocity field that arises due to an external force $\boldsymbol{F}$. A common way to solve Stokes flow (also called creeping flow) problems is to use Green's functions, which are known for a point force:

$$\boldsymbol{f}(\boldsymbol{r}) = \boldsymbol{f}_0 \delta(\boldsymbol{r} - \boldsymbol{r}') \tag{2}$$

The solution for the velocity field due to a single perturbation acting on a point $\boldsymbol{r}'$ can be written as

$$\boldsymbol{v}(\boldsymbol{r}) = \boldsymbol{T}(\boldsymbol{r} - \boldsymbol{r}') \cdot \boldsymbol{f}_0, \tag{3}$$

with $\boldsymbol{T}$ the Oseen tensor, given by

$$\boldsymbol{T}(\boldsymbol{r}) = \frac{1}{8\pi\eta r}\left(\boldsymbol{I} - \frac{\boldsymbol{r}\boldsymbol{r}}{r^2}\right) \tag{4}$$

Due to the linearity of Eq. (1), solutions to more complex problems can in principle be obtained by superposition of these fundamental solutions. Other approaches rely on integral expressions of the Stokes equation. In particular, the Boundary Element Method is often used to solve the fluid flow around bodies with arbitrary geometries [2].

Problems in fluid dynamics are generally quite involved to solve, even numerically. In computational fluid dynamics (CFD), grid-based methods are frequently used, and their achievements are remarkable. Depending on the problem, either Eulerian meshes or Lagrangian meshes are used, both with their advantages and pitfalls. Eulerian grid methods, such as the Finite Volume Method (FVM), are versatile in CFD, though their use of a fixed grid in space results in difficult free surfaces tracking while mesh generation might pose problems as well. In addition, the advection term in NS can lead to numerical diffusion problems. Lagrangian methods on the other hand, attach their grid to the moving material, and do not suffer from these problems. Unfortunately, expensive mesh regeneration becomes inevitable when dealing with large deformations. Therefore, Lagrangian methods are usually applied in solid mechanics. Despite their accuracy, the use of grid-based methods generally leads to difficulties in problems with free surfaces, large deformations, and discontinuities.

Over the last decades, there has been a strong increase of interest in *meshless methods* to solve the governing PDEs. Briefly, these methods compute the field variables and respective derivatives by use of a kernel interpolant which applies to the surrounding points lying in a sphere of influence determined by a cutoff distance. The neighboring points (particles) can move both in and out of this

sphere. All properties are carried by the particles. As such, some pitfalls that are inherent to mesh-based methods, largely disappear in meshless methods.

Nowadays, one of the most popular meshless methods to model fluid dynamics is Smoothed Particle hydrodynamics[1] (SPH). SPH is a purely Lagrangian method, and while largely used in violent situations such as wave impact, astronomical phenomena, and explosions, applications are also abundant in low speed dynamics, e.g. water transport in porous media, surface tension modeling, multi-phase flow, and diffusion, e.g [4, 5, 6, 7, 8, 9]. Additionally, SPH can be applied in biological systems where one typically encounters non-Newtonian liquids, viscoelastic liquids, and in microscopic systems, thermal fluctuations [10, 11, 12]. Due to its particle nature, it has also interesting links with molecular dynamics (MD) [3]. Although most SPH simulations are quite robust and can deal with discontinuities in a natural way, there are some notable downsides, too: SPH methods can suffer from instabilities (mostly due to particle clustering), while their accuracy can be inferior to mesh-based methods. There are several correction mechanisms available and still being developed to cope with these problems [13, 14], yet usually at the expense of a substantially higher computational cost. Nevertheless, the big advantage of SPH is that a wide range of physical aspects are relatively easy implemented in a particle simulator. As such, SPH is a powerful and flexible tool to tackle a wide range of multi-physics problems [15].

As mentioned above, SPH simulations can be used to investigate microscopic environments such as cellular systems [16, 17, 18]. In this regard, other models with a particle nature trying to capture the motion of cells and sub-cellular systems over longer timescales have been proposed, but they usually rely on a description with overdamped Maxwellian elements, and the parameters in these models need to be calibrated or scaled to properly incorporate the fluid dynamics [19, 20]. Yet, since SPH is essentially a discretization technique of the Navier-Stokes equations, this will put restrictions on the feasibility of the solution. Microscopic problems generally require a small time-stepping algorithm, while the timescale of the whole system may cover several orders of magnitude ($\succ 10^9$) of this time-step. In the context of stability, explicit algorithms in SPH are restricted by the CFL criterion, i.e.

$$\delta t \leq 0.25 \frac{h}{c}, \tag{5}$$

where h is the smoothing length, which defines the interaction cutoff between two particles, and c is the speed of sound in the medium. Due to the parabolic term in NS, the viscous diffusion also poses restrictions:

$$\delta t \leq 0.125 \frac{h^2 \rho}{\mu}, \tag{6}$$

[1] In principle the joint name for meshless solid, gas and fluid related applications is termed Smoothed Applied Particle Mechanics (SPAM) [3].

where ρ is the density and μ is the dynamic viscosity of the medium. Finally, the particle accelerations a also constrain the time-step by

$$\delta t \leq 0.25 \min_a \left(\frac{h}{a} \right)^{\frac{1}{2}}. \tag{7}$$

Which criterion actually poses the restriction depends on the problem [21]. However, since c can be assumed small in a low Reynolds number context, it is mostly imposed by Eq. (6). Let us consider the example of a cell moving in a fluid. If the cell is discretized by particles with a realistic spacing of $\sim 0.1\,\mu$m in an aqueous medium ($\mu = 5\,\text{mPa}\cdot\text{s}$) one arrives at $\delta t \leq 10^{-9}\,\text{s}$. This implies a huge number of calculations if the timescale of interest is of the order of 1 s. Other cases may be found in microfluidics applications or liquid flow through a porous medium.

To cope with the insurmountable problem of viscous diffusion using explicit time integration, implicit schemes in SPH have been introduced. Litvinov et al. (2010) [22] proposed a splitting integration scheme to deal with the high Schmidt numbers in mesoscopic SPH simulations, although earlier research in that direction was already conducted by Monaghan (1997) [23] for SPH simulations in gas dynamics. Fan et al. (2010) [24] used a Generalized Minimal Residual method to model highly viscous moulding flows.

In contrast to the approaches above, the key idea in this paper is to start from the Stokes equations formulated in the SPH context. We will term the solution method to solve these equations as *NSPH*, where the N refers to non-inertial. In section 3, we will explain how Eq. (1) can be solved efficiently, and point out the differences with the standard SPH formulation (section 2). We show with a number of examples (section 4) that the problems mentioned earlier can be simulated accurately with a much larger time-step, resulting in lower computational time compared to standard SPH.

2. Standard SPH formulation

We start from the isothermal hydrodynamic equations in Lagrangian form which can be written as

$$\frac{D\boldsymbol{v}}{Dt} = \frac{1}{\rho}\nabla \cdot \boldsymbol{\sigma}, \tag{8}$$

and

$$\frac{D\rho}{Dt} + \rho \nabla \cdot \boldsymbol{v} = 0, \tag{9}$$

representing the momentum equation and the density continuity equation respectively. In these equations, ρ and $\boldsymbol{\sigma}$ represent the fluid density and the stress tensor. The stress is in turn expressed as

$$\boldsymbol{\sigma} = -\boldsymbol{P} + \boldsymbol{\tau}, \tag{10}$$

where $\boldsymbol{P}$ is the hydrostatic pressure tensor and $\boldsymbol{\tau}$ is an extra deviation stress tensor. In case we are dealing with a Newtonian fluid, then $\boldsymbol{\tau} = 2\mu\boldsymbol{D}$ where μ is the viscosity of the fluid and $\boldsymbol{D}$ the strain rate tensor.

In SPH, the basic idea is to approximate a function evaluation associated to a particle, $f(\boldsymbol{x}_i)$, by a set of neighboring particles j, expressed as

$$f(\boldsymbol{x}_i) \approx \sum_j \mathcal{V}_j f(\boldsymbol{x}_j) W_{ij}, \tag{11}$$

where $\boldsymbol{x}_i$ is the position of the particle, and $\mathcal{V}_i$ is the volume occupied by one particle. The approximation function is a kernel $W_{ij} \equiv W(q,h)$ were $q = r_{ij}/h$, r_{ij} is the distance from a particle i to another fluid particle j, and h is the smoothing length, representing the domain over which the particle i has interaction with particles j. It is symmetrical, i.e.

$$W_{ij} = W_{ji}, \tag{12}$$

and should be normalized:

$$\int_{\mathcal{V}} W d\mathcal{V} = 1. \tag{13}$$

Unlike in FEM, where the particle mesh is a fixed topology, the SPH interpolation function W_{ij} is a MD-like potential which allows particles to move in and out of the interaction area with particle i. In this paper we initially consider a cubic spline function $W(q,h)$ as a kernel function, which reads

$$W(q,h) = \frac{2}{3\pi h^3} \begin{cases} \frac{2}{3} - q^2 + \frac{1}{2}q^3 & 0 \le q \le 1 \\ \frac{1}{6}(2-q)^3 & 1 < q \le 2 \\ 0 & q > 2 \end{cases} \tag{14}$$

Despite its polularity and history in SPH, the cubic spline usually does not yield the most stable or accurate results. It was found by Morris et. al (1999) [21] that the quintic B-spline, defined by

$$W(q,h) = \frac{7}{478\pi h^2} \begin{cases} (3-q)^5 - 6(2-q)^5 + 15(1-q)^5 & 0 \le q \le 1 \\ (3-q)^5 - 6(2-q)^5 & 1 < q \le 2 \\ (3-q)^5 & 2 < q \le 3 \\ 0 & q > 3 \end{cases} \tag{15}$$

yields significantly better results, which are linked to the properties of the Fourier transform of the kernel (the more positive and decreasing for increasing wave numbers, the better) [25]. In this regard, the Wendland kernel, defined by

$$W(q,h) = \frac{7}{4\pi h^2} \begin{cases} (1-\frac{q}{2})^4(1+2q) & 0 \le q \le 2 \\ 0 & q > 2 \end{cases} \tag{16}$$

should be an even better choice.

In the Navier-Stokes equations, a continuous force field $\boldsymbol{F}$ can be decomposed in a conservative pressure driven $\boldsymbol{F}^p$ and a viscous component $\boldsymbol{F}^v$. A

fluid particle i in SPH moves accordingly to a discretization of NS for a set of surrounding particles j, which for the pressure component $\boldsymbol{F}^p$ can be computed by

$$\boldsymbol{F}_i^p = -m_i \sum_j m_j \left(\frac{P_i}{\rho_i^2} + \frac{P_j}{\rho_j^2} \right) \nabla_i W_{ij}. \tag{17}$$

For the viscous forces, there are several formulations. A frequently used friction term for laminar flows was first introduced by Morris et al. (1999), and reads (hereafter called V-MR):

$$\boldsymbol{F}_i^v = m_i \sum_j m_j \left(\frac{\mu_i + \mu_j}{\rho_i \rho_j} \right) \frac{1}{r_{ij}} \frac{\partial W_{ij}}{\partial r_{ij}} \boldsymbol{v}_{ij}. \tag{18}$$

Another formulation is derived from the artificial viscosity implementation for SPH to model shock waves, and was first introduced by Monaghan [26] (hereafter called V-MG)

$$\begin{aligned} \boldsymbol{F}_i^v &= m_i \sum_j \chi \frac{m_j}{\rho_i \rho_j} \left(\frac{\mu_i \mu_j}{\mu_i + \mu_j} \right) \nabla_i W_{ij} \frac{\boldsymbol{r}_{ij} \cdot \boldsymbol{v}_{ij}}{r_{ij}^2} \\ &= m_i \sum_j \chi \frac{m_j}{\rho_i \rho_j} \left(\frac{\mu_i \mu_j}{\mu_i + \mu_j} \right) \frac{1}{r_{ij}} \frac{\partial W_{ij}}{\partial r_{ij}} (\boldsymbol{v}_{ij} \cdot \boldsymbol{e}_{ij}) \boldsymbol{e}_{ij}, \end{aligned} \tag{19}$$

where we have defined $\boldsymbol{e}_{ij} = \frac{\boldsymbol{r}_{ij}}{r_{ij}}$. In these equations, m_i are the particle masses and $\boldsymbol{v}_{ij}$=$\boldsymbol{v}_i$-$\boldsymbol{v}_j$ and $\boldsymbol{r}_{ij}$=$\boldsymbol{r}_i$-$\boldsymbol{r}_j$ denote the relative particle velocity and positions respectively. The value of the constant χ depends on the kernel type and will be determined later on. Note the difference in both formulations: in Eq. (18) $\boldsymbol{v}_{ij}$ is multiplied by a friction factor, while in Eq. (19), only the projection of $\boldsymbol{v}_{ij}$ on the inter-particle vector $\boldsymbol{r}_{ij}$ contributes to the forces.

In the so-called weakly compressible SPH approach, it is convenient to use the following equation of state (EOS) [27] to have a closing relation between the pressure and the density:

$$P = P_0 + \kappa \left[\left(\frac{\rho}{\rho_0} \right)^7 - 1 \right], \tag{20}$$

where P_0 is the initial net pressure, ρ_0 is the initial density of the fluid, and $\kappa = \frac{\rho_0 c^2}{7}$ is the compression modulus where c is the speed of sound of the medium. Eq. (20) enables us to handle free surfaces of the liquid. Small variations in density will be penalized by an increased pressure, thus making the fluid weakly compressible. Finally, to update the density, we use the SPH approximation of the continuity equation

$$\frac{D\rho_i}{Dt} = \sum_j m_j \boldsymbol{v}_{ij} \cdot \nabla_i W_{ij}. \tag{21}$$

The equations which need to be integrated in standard fluid mechanics are Eq. (21) and

$$m_i \dot{\boldsymbol{v}}_i = \boldsymbol{F}_i^p + \boldsymbol{F}_i^v + \boldsymbol{F}_i^b + \boldsymbol{F}_i^e, \tag{22}$$

i.e. Newton's equation of motion, where $\boldsymbol{F}_i^b$ and $\boldsymbol{F}_i^i$ are additional body forces and internal forces to account for other physical aspects in the system. Eq. (22) can be solved with a second order Verlet numerical scheme (which is known for its energy conserving properties) though there are higher order schemes present in literature [3]. The continuity equation is solved by an explicit Euler scheme.

3. SPH formulation for Stokes flow

Let us now assume a system that is friction dominated so that we can explicitly omit the inertial term in Eq. (22). If one considers the friction model Eq. (18), the resulting creeping flow equations read:

$$\begin{aligned} -m_i \sum_j m_j \left(\frac{\mu_i + \mu_j}{\rho_i \rho_j}\right) \frac{1}{r_{ij}} \frac{\partial W_{ij}}{\partial r_{ij}} \boldsymbol{v}_{ij} = m_i \sum_j m_j \left(\frac{P_i}{\rho_i^2} + \frac{P_j}{\rho_j^2}\right) \nabla_i W_{ij} \\ + \boldsymbol{F}_i^b + \boldsymbol{F}_i^e. \end{aligned} \tag{23}$$

Introducing the volume $\mathcal{V}_i = m_i/\rho_i$ and assuming for simplicity that $m_i = m_j$, we can write this in a condensed form as

$$\begin{aligned} -\sum_j \Gamma_{ij} \boldsymbol{v}_{ij} &= m_i \sum_j m_j \left(\frac{P_i}{\rho_i^2} + \frac{P_j}{\rho_j^2}\right) \nabla_i W_{ij} + \boldsymbol{F}_i^b + \boldsymbol{F}_i^e \\ &= \sum_j \left(P_i \mathcal{V}_i^2 + P_j \mathcal{V}_j^2\right) \nabla_i W_{ij} + \boldsymbol{F}_i^b + \boldsymbol{F}_i^e, \end{aligned} \tag{24}$$

with the friction matrix Γ defined as

$$\Gamma_{ij} = (\mu_i + \mu_j) \frac{\mathcal{V}_i \mathcal{V}_j}{r_{ij}} \frac{\partial W_{ij}}{\partial r_{ij}}. \tag{25}$$

In a more general form, we can write the impulse equation as

$$-\sum_j (\Gamma_{ij}^{\perp} \boldsymbol{v}_{ij}^{\perp} + \Gamma_{ij}^{\parallel} \boldsymbol{v}_{ij}^{\parallel}) = \sum_j \left(P_i \mathcal{V}_i^2 + P_j \mathcal{V}_j^2\right) \nabla_i W_{ij} + \boldsymbol{F}_i^b + \boldsymbol{F}_i^e, \tag{26}$$

where we have introduced the perpendicular and parallel velocity vectors $\boldsymbol{v}_{ij}^{\parallel} = (\boldsymbol{v}_{ij} \cdot \boldsymbol{e}_{ij}) \boldsymbol{e}_{ij}$, $\boldsymbol{v}_{ij}^{\perp} = \boldsymbol{e}_{ij} \times (\boldsymbol{e}_{ij} \times \boldsymbol{v}_{ij})$ respectively. In this regard, the friction formulation (19) has $\Gamma_{ij}^{\perp} = 0$. In SPH, this formulation has the advantage that it conserves the angular momentum of the system [26].

The linear system (Eq. (26)) needs to be solved by inversion of the friction matrix to obtain $\boldsymbol{v}_i$. Although this appears to be a very expensive operation at first glance, the matrix Γ is very sparse: the particles only interact with a limited number of neighbors. This enables us to use an efficient iterative solution

procedure: The Conjugate Gradient Method (CGM) is an obvious candidate for this, provided that the matrix is symmetric and positive definite [28]. Since all interactions in the particle system are symmetric, the first condition is automatically fulfilled. The second condition is also fulfilled - here, we refer to Appendix A for the derivation. After using a Jacobi preconditioner, the condition number of Γ is close to 1, allowing for very quick convergence of the CGM solution. If the system is solved, all that remains is a set of first order equations that can be solved with an explicit Euler scheme.

3.1. Numerical stability of NSPH

Since the PDE Eq. (1) lacks time-evolution, the viscous diffusion criterion and the Courant condition vanish. Hence, another time advancing algorithm will be adopted. Compared to the second order system in standard SPH, the solution of Eq. (26) is quite expensive. CGM is an iterative procedure and requires an efficient handling of the data structure of the particle contact containers. Whether the CGM converges sufficiently depends on the applied forces and the convergence criterion for the velocity $\phi = \max\{\boldsymbol{v}_{n+1} - \boldsymbol{v}_n\}$. However, if convergence is sufficient for a single operation, we are left with updating the particle positions:

$$\dot{\boldsymbol{x}}_i = \boldsymbol{v}_i. \tag{27}$$

For a linear system described by

$$-\gamma \dot{\boldsymbol{y}}_i = k\boldsymbol{y}_i, \tag{28}$$

with γ, $k \succ 0$, the numerical stability for an explicit Euler scheme with time-step δt is ruled by the condition

$$\delta t \prec \frac{\gamma}{k}. \tag{29}$$

How does this relate to the NSPH formulation? If we ignore the body forces and other forces for the moment, and recall that in the equation of state (20), we have that $P \sim \kappa$, the criterion for the SPH analogon Eq. (24) can be expected to take the form

$$\delta t = \alpha \min_i \left(\frac{\mu_i}{\kappa_i} \right), \tag{30}$$

where α is a dimensionless factor to be determined and assumed to be constant. There are two important aspects of this criterion. Contrary to the criterion for viscous diffusion Eq. (6) for the original SPH equations, an increase in viscosity improves the stability of the method. As given by Eq. (5)-(6), the speed of sound and viscosity pose their own restrictions on SPH, whereas here, the compression modulus and viscosity counterbalance each other. A second advantage is that the criterion is not related to the smoothing length, owing to the fact that the kernel derivatives in Eq. (23) basically cancel each other out. This is an important advantage over criterion Eq. (6) which poses a quadratic decrease of the time-step with the smoothing length. These considerations allow us to use a relatively large time-step.

Finally, we mention that the additional forces between particles $\boldsymbol{F}^e$, which can be regarded as viscoelastic pair potential interactions or bonds, need to be decomposed in a conservative part and a dissipative part. These parts contribute in Eq. (30) to the denominator and nominator respectively and might put additional restrictions on the time-step (see section 4.5).

4. Numerical tests and examples

In the following sections, we illustrate the effectiveness of the method by comparison with normal SPH simulations. We do this by means of three classical examples: Poiseuille flow, the lid driven cavity problem, and the flow past cylinders. We also demonstrate the extension capabilities by superimposing elastic interactions to determine the relaxation time of a deformed cell and to simulate the red blood cell motion in a Poiseuille flow.

4.1. Boundary conditions

The implementation of the appropriate boundary conditions can be non-trivial for SPH [29]. A straightforward implementation of boundary conditions in SPH is to"freeze" the boundary particles. This means that these particles do not update their momentum, though their density is updated according to Eq. (21). This is a zeroth order approximation of no-slip boundaries, since the interpolated velocity at the edge of a boundary might not be equal to the velocity of an edge particle. An elegant solution to this is to assign mirroring velocities to a boundary particle if a fluid particle approaches [21]. This velocity is purely virtual, as it does not update the positions of the boundary particle. It alters the interaction with the fluid particles in such a manner that the velocity field at the boundary is exactly zero. In this work, however, we will not concentrate on the accuracy of boundary conditions and use the method of frozen particles, which yields acceptable and insightful results. To "freeze" the boundary particles, we assign a very high friction coefficient to them. This ensures that the CGM will find their velocities to be zero (see also Appendix A).

4.2. Poiseuille flow

This classical test consists of a fluid moving between two infinitely long parallel plates under a constant body force. The plates are at a distance $L = 1\,\mathrm{mm}$ while the fluid has a viscosity of $\mu = 1\,\mathrm{mPa}\cdot\mathrm{s}$ and a density of $\rho = 1000\,\mathrm{kg/m^3}$. The force acting on the particles is set to $F_x = 10^{-4}\,\mathrm{N}$. The fluid speed of sound is initially set to $c = 0.06\,\mathrm{ms}^{-1}$, thus associated with a compressibility modulus of $\kappa = 0.5\,\mathrm{Pa}$. The particle system has a resolution of $2.5 \times 10^{-5}\,\mathrm{m}$ with a total of $40{\times}40$ fluid particles and periodic boundary conditions which are imposed to the x direction and implemented using ghost particles. In all further simulations, a fixed smoothing length h of $1.3\times$ the particle spacing is used for the cubic spline and Wendland kernel, and $0.8667\times$ for the quintic spline to cover a sufficient number (> 20) of neighboring particles.

After an initial transient behavior, the steady state solution for the velocity profile parallel to the plates is given by:

$$V_x = \frac{\rho F_x}{2\mu} y(y - L). \tag{31}$$

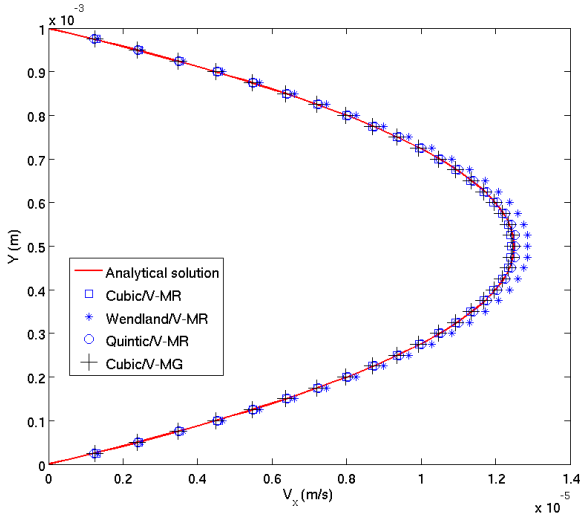

Figure 1: NSPH Poiseuille flow velocity profiles after 1 time-step, obtained with different kernels and viscous models. The analytical solution is also given.

This corresponds to a peak velocity $V_x = 1.25 \times 10^{-5}\,\mathrm{m/s}$, and hence $Re = 0.0125$. We have run simulations using SPH and NSPH for the two viscosity models mentioned above. For SPH, the time-step is set to $5 \times 10^{-5}\,\mathrm{s}$. In this system a steady state flow is reached after $t = 0.5\,\mathrm{s}$, thus bridging about 10000 time-steps in the case of SPH. In contrast, the NSPH simulation requires only one time-step to reach steady state (CGM residual error tolerance is set to $\phi = 10^{-10}\,\mathrm{m/s}$). For the NSPH simulations, the minimal time-step depends on the viscosity model. For the viscous models V-MG and V-MR, we empirically found $\alpha_1 = 0.25$ and $\alpha_2 = 0.1$ respectively, resulting in $\delta t_1 = 5 \times 10^{-4}\,\mathrm{s}$ and $\delta t_2 = 2 \times 10^{-4}\,\mathrm{s}$ to run a stable simulation over 10^5 time-steps[2].

The analytical solution can be viewed in Fig. 1, together with the numerical results obtained with a combination of different kernels and viscous models. The optimal value χ for each kernel can be retrieved in Table 1. We only display all the results for V-MR, and the profile using V-MG and the cubic kernel. All runs are in very good agreement with the analytical solution, except for the combination V-MR with Wendland kernel.

[2]To find the steady state solution only, a larger time-step may be used as well.

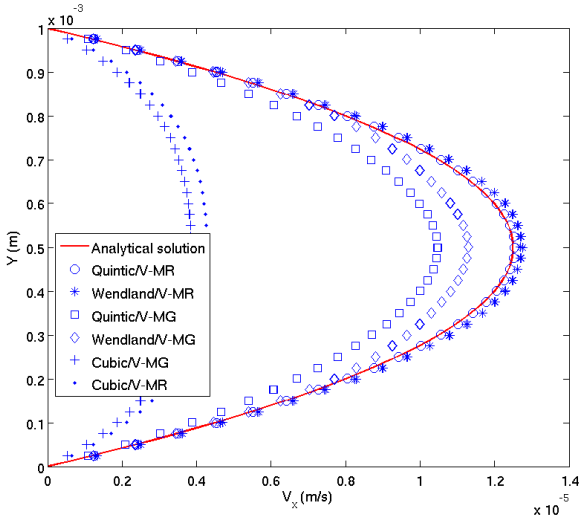

Figure 2: NSPH Poiseuille flow velocity profiles after 10^5 time-steps, obtained with different kernels and viscous models.

Model	C/V-MR	C/V-MG	W/V-MR	W/V-MG	Q/V-MR	Q/V-MG
Timestep [s]	2×10^{-4}	5×10^{-4}	2×10^{-4}	5×10^{-4}	2×10^{-4}	5×10^{-4}
Scaling factor χ	-	9.25	-	9.91	-	11.41
RE (0 steps), %	0.7	**0.3**	3.1	**0.3**	0.4	**0.3**
RE (10^5 steps), %	60	65	3.5	8.1	**0.5**	16
CPU time (t=20s) [s]	4200	2200	3200	1200	2000	**900**

Table 1: Values summarizing the NSPH results for Poiseuille flow obtained with different kernels and viscous models. The optimal scaling factors χ for the viscous models Eq. (18) and Eq. (19) are based on this example. The relative errors (RE) compared to the analytical solution are given for 1 time-step and after 10^5 time-steps, while the CPU time required is indicated as well. The boldfaced numbers indicate the best result.

Let us then turn to a situation which requires a longer time period. It is evident that the model results should not vary too much in time. Therefore, we have continued the runs to 10^5 time-steps. The results, depicted in Fig. 2 show an interesting evolution. The profiles obtained with the cubic spline have clearly deviated from the analytical solution in a matter that they have become unusable. This happens in particlular after roughly 10000 time-steps. Fortunately, this numerical diffusion is less prominent in the results for the Wendland and quintic spline using V-MG, and hardly visible when using V-MR (see Table 1, RE). For the latter choice, one additional simulation covering 10^6 time-steps ($t = 200\,\mathrm{s}$) did not yield any significant increase of the error. Thus, the effect of the kernel choice seems to be of utmost importance. Table 1 further indicates that simulations with viscous model V-MG are about two times faster compared to V-MR, due to the larger time-step that can be used.

A related aspect is the influence of κ in the equation of state. In SPH, a higher speed of sound can cause an artificial increase of the viscosity in the particle system. Hence, κ needs to be taken sufficiently large so that particle interactions are strong enough to mimic the incompressibility, yet low enough to prevent the effect on viscosity. In our NSPH simulations, there seems to be a similar effect. However, using a cubic spline, we find that a variation in κ can significantly change the velocity profiles, while the Wendland and quintic kernels are less sensitive to κ. We will not discuss these aspects in further detail, but based on these primary insights, retain only the quintic kernel with fixed κ in each of the following examples.

4.3. Shear driven cavity and Couette flow

The shear driven cavity consists of a fluid-filled rectangular box with a top plate moving at constant horizontal velocity, creating a vortex near the shearing boundary. The box has dimension $L = 10\,\mu$m while the fluid has a viscosity of $\mu = 1\,\text{mPa}\cdot\text{s}$ and a density of $\rho = 1000\,\text{kg/m}^3$. The plate particles are moving with at a speed of $V_x = 5\,\mu$m/s. This corresponds to $Re = 5 \times 10^{-5}$. As in the previous example, we set $\kappa = 0.5\,$Pa. The initial particle system has a resolution of $0.4\,\mu$m with a total of 625 fluid particles (Fig. 3). A time-step of $2 \times 10^{-4}\,$s is used. The velocity profiles of this system are obtained by monitoring the horizontal velocities (V_y) at the center of the box.

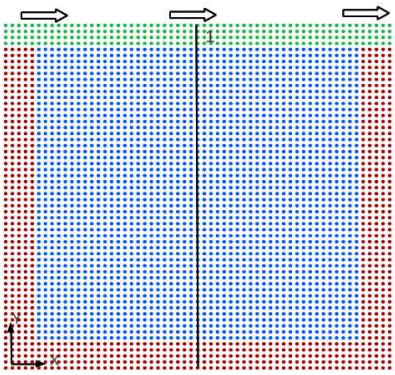

Figure 3: Particles representing the shear driven cavity problem. The vertical line indicates the postions of the particles at which the velocity profile is taken.

Contrary to the Poiseuille flow example, and against the philosophy of *instant* action, we find that the NSPH method requires more than one time-step to reach the steady state (despite the low Reynolds number). In Fig. 4, we display the velocity profile for a number of time-steps, indicating that an acceptable result is obtained after about a minimum of 5 time-steps[3]. Interestingly, we

[3]We stress that this is not the number of iterations required to obtain convergence in the

found that an increased viscosity impairs the convergence, but can be compensated by using a larger incompressibility. The NSPH simulations thus needs a minimal compressibility –which depends on the viscosity– in order to get a quick, satisfying solution.

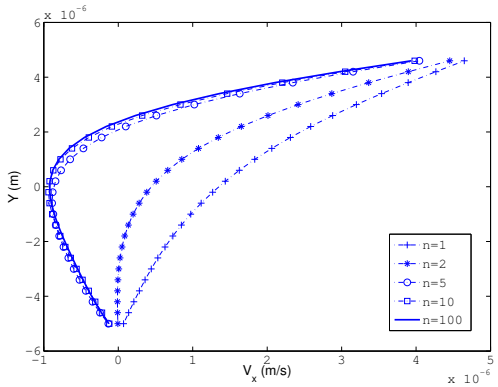

Figure 4: Steady state velocity profile in the shear driven cavity for a spatial resolution of $0.4\,\mu m$ obtained with NSPH (quintic/V-MR) after a number of time-steps n. The profile converges after roughly 5 to 10 time-steps.

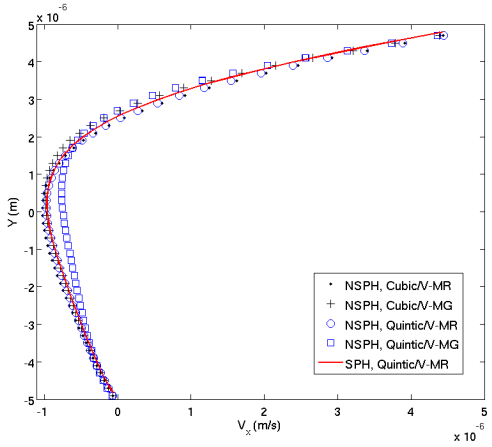

Figure 5: Steady state velocity profile in the shear driven cavity for a spatial resolution of $0.2\,\mu m$ generated with NSPH using quintic and cubic kernels (obtained after 10 time-steps), and with SPH, using a quintic kernel and V-MR (obtained after 10000 time-steps).

Emphasizing on the difference with the Poiseuille flow example, where all particles get nearly equal forces and hence convergence is found directly, this is

Conjugate gradient Method.

not the case here because the interaction forces are initially only present in the area near the moving wall. To investigate this further, we considered a simpler shearing system without the vertical walls (Couette flow), generating a linear stationary velocity profile,

$$V_x = \frac{V_0}{L} y. \tag{32}$$

In this case, the NSPH simulations do capture the exact profile from the first time-step on. This means that the velocities near the bottom wall as derived from CGM, are immediately equilibrated with those imposed from the top plate. The issue is further neither related to the spatial scale of the system, as a twice as high resolution basically yields the same behavior, nor to the temporal scale, as a decreased time-step cannot solve the problem either. Thus, it seems that the problem is caused by the geometry of the system (see also section 4.4), and the nonlinear velocity profiles that arise from it.

We also want to refer to the time-step used in NSPH not being dependent on h. Fig. 5 depicts the results obtained with a particle spacing of $0.2\,\mu$m using the same time-step. The NSPH result (after 10 time-steps) using quintic/V-MR is in very good agreement with the standard SPH (quintic/V-MR) steady state solution, which requires a time-step of 5×10^{-9} s (due to limitations for viscous diffusion). Other NSPH runs using a cubic spline and V-MG are given as well, indicating a close mutual agreement, though less for the quintic kernel in combination with V-MG.

4.4. Flow past an array of cylinders

In this system, which can be regarded as a basic 2D representation of a flow through a porous medium, we consider a fixed cylinder immersed in a fluid between two parallel plates. The problem has periodic boundaries in the x direction, and hence represents an infinitely long array with equally spaced cylinders (see Fig. 6). The plates are at a distance $L = 1 \times 10^{-2}$ m and the radii of the cylinders are $R = 4 \times 10^{-3}$ m. The fluid has a viscosity of $\mu = 5\,\text{mPa} \cdot \text{s}$ and is driven by a body force of $2.2 \times 10^{-4}\,\text{ms}^{-2}$. The particles are initially positioned on a square lattice using a spacing of 6.7×10^{-5} m ($h = 5.8 \times 10^{-5}$ m), with those representing the cylinders being restricted by R. The Reynolds number is approximately 0.02. The simulations are run arbitrarily choosing $\kappa = 2\,\text{Pa}$ (equivalent $c = 0.12\,\text{m/s}$), a time-step of 2×10^{-4} s, and using the viscous model V-MR combined with the quintic kernel. The CGM residual error tolerance is set to $\phi = 5 \times 10^{-9}\,\text{m/s}$. The velocity profiles along paths 1 and 2 are shown in Fig. 7 and Fig. 9 for the NSPH simulations and are compared with the standard SPH steady-state solution (obtained after 15000 time-steps, using $c = 0.015\,\text{m/s}$). Similarly as in the shear driven cavity, the NSPH results are in very close agreement with the SPH runs, though are obtained after a minimum number of time-steps (n$\geq$10).

It may now be objected that the results from the examples above are valid for uniform particle distributions, but do not refer to realistic situations where the particles have been advected and the kernel interpolation becomes usually

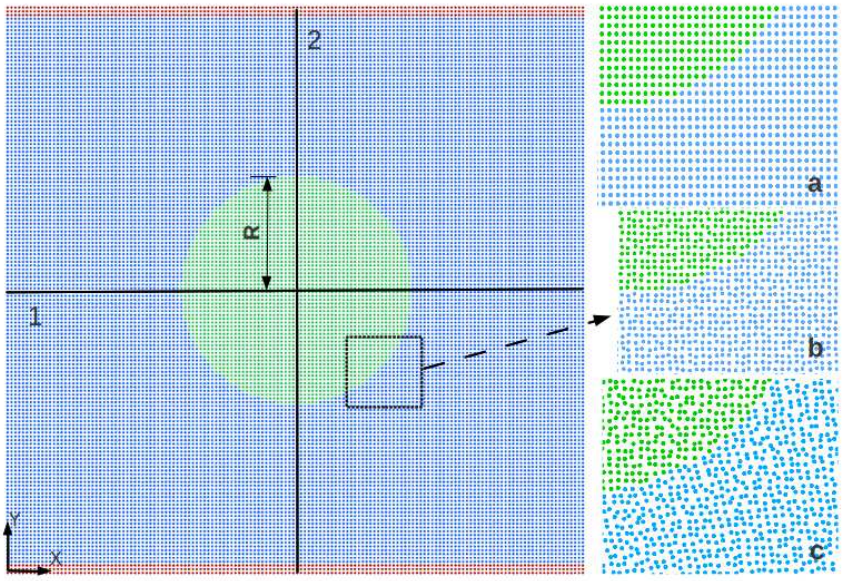

Figure 6: Particle system representing the flow past an array of cylinders. The vertical and horizontal lines indicate the postions of the particles at which the velocity profiles are taken. On the right side we indicate the used distorted particle configuration (a: none, b: moderate, c: high).

less accurate. To address this, we have increased the challenges, and created an initial situation where the particles are not spaced regularly. The particle positions were distorted by adding a uniformly distributed "moderate" random component of $\pm 1 \times 10^{-5}$ m (15% of the inital spacing) and "high"one of $\pm 1.7 \times 10^{-5}$ m (25% of the inital spacing). In addition the simulations were run over 10^6 time-steps, thus moving the particles away from their initial positions. In Fig. 9, we depict the new velocity profile along line 2, indicating that the NSPH results are quite equivalent to those of SPH. In the ordered particle configuration, effects of numerical diffusivity are present both for SPH and NSPH after 10^6 time-steps, though apparently less for NSPH. On the other hand, the profiles obtained from the distorted configurations show little multual differences (for the sake of clarity, the profiles from the moderate configuration are not shown). Additionally, we found that the NSPH required CPU time did not depend on the degree of particle disorder, with a rather steady convergence time per timestep. We want to emphasize though, that these results are only meant as a direct comparison of SPH and NSPH for three initial cases of particle configurations. The intrinsic accuracy and convergence of SPH in this example depends on the particle discretization, spatial configuration, and the smoothing length [30].

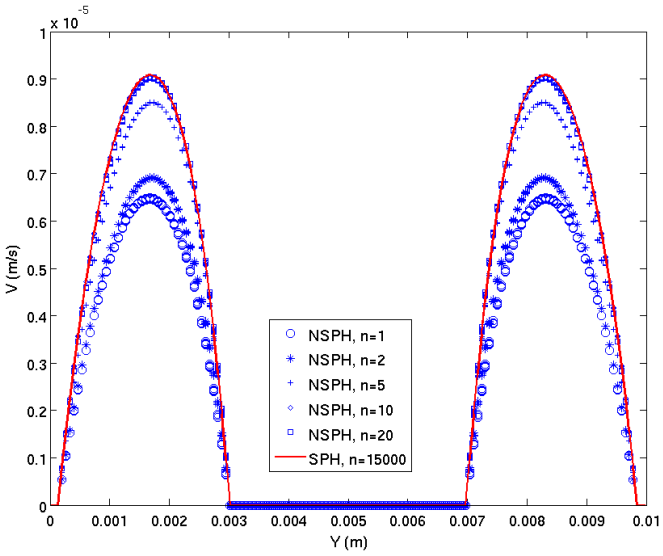

Figure 7: Simulated velocity profile with NSPH along line 2, for an increasing number of time-steps n (comparison with SPH also shown).

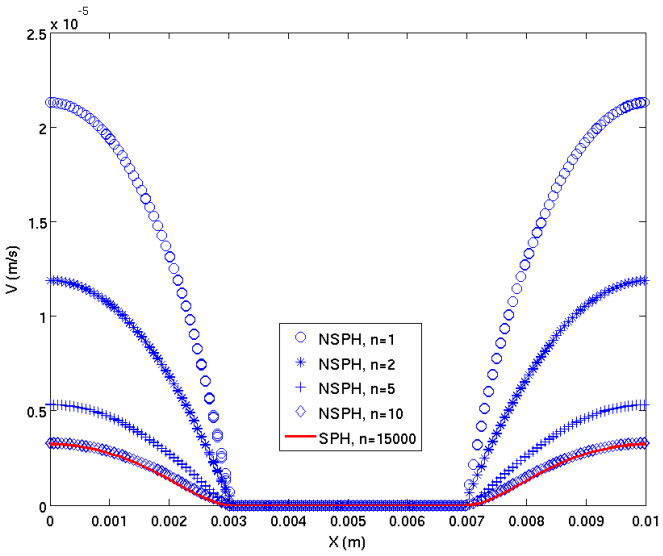

Figure 8: Simulated velocity profile with NSPH along line 1, for an increasing number of time-steps n (comparison with SPH also shown).

4.5. Relaxation of a stretched red blood cell immersed in fluid

Red blood cells (or erythrocytes) are flexible membrane structures designed to flow efficiently in the cardiovascular system of mammals. In the literature,

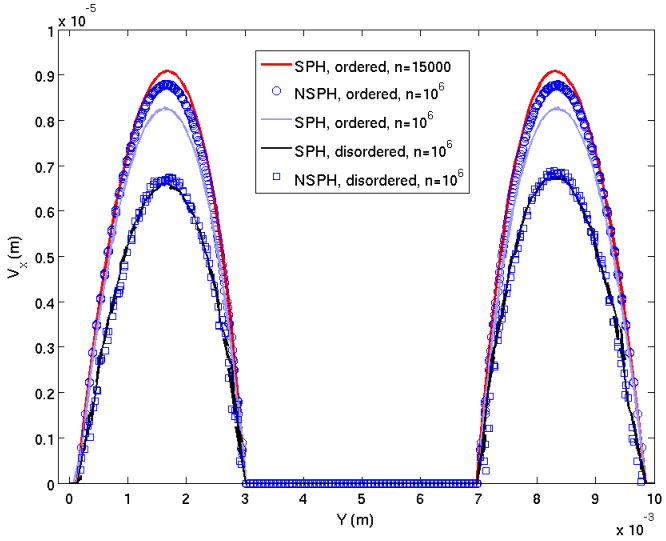

Figure 9: Simulated velocity profile with NSPH and SPH and along line 2, obtained after 10^6 time-steps for an initial ordered and heavily distorted particle configuration.

there is quite a lot of recent work detailing the underlying constitutive laws of the RBC membrane, using experimental stretching with optical tweezers, and the numerical modeling hereof [31, 32, 33, 34]. In this work however, we start from a stretched cell and only focus on the relaxation times. This kind of experiment is well suited to give insight into the initial viscoelastic behavior of the membrane and cortical cytoskeleton, as well as the subsequent (long-term) cytoskeletal changes [32]. We consider a red blood cell immersed in plasma, and suppose we perform an experiment in which the cell is stretched with an optical tweezer.

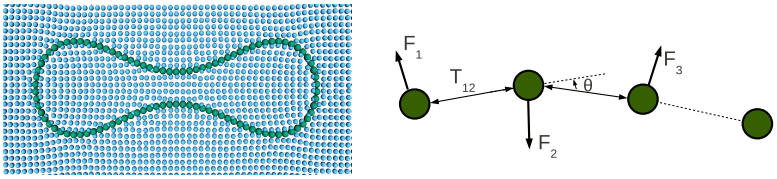

Figure 10: Relaxed RBC shape and detail of the forces acting on a particle trio.

The shape of a RBC (see Fig. 10, left) in equilibrium can be approximated mathematically as a biconcave disc, in 2D described by the following equation:

$$y = 0.5\,(1-x^2)^{1/2}\,(c_0 + c_1 x^2 + c_2 x^4), \quad -1 \le x \le 1, \tag{33}$$

with $c_0 = 0.207$, $c_1 = 2.002$, and $c_2 = -1.122$. The coordinates are scaled according to the the radius r_0 which is approximately $3.9\,\mu$m for a human RBC.

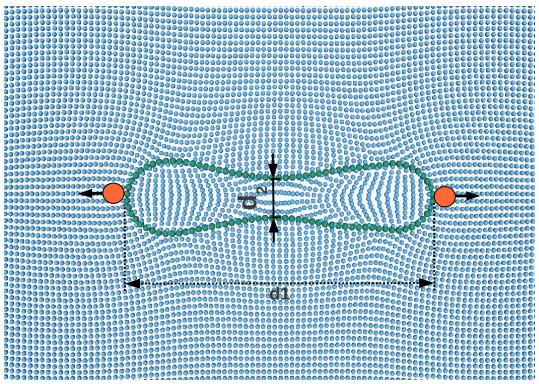

Figure 11: Snapshot of the initial RBC configuration: The cell is stretched by the optical tweezer traps (red circles). There are about 10000 particles in this system.

The constitutive in-plane stress-strain function for the membrane can be computed by

$$E = \frac{E_s}{4}(\frac{1}{2}I_1^2 + I_1 - I_2) + \frac{E_d}{8}I_2^2, \tag{34}$$

in which $I_1 = \lambda_1^2 + \lambda_2^2 - 2$ and $I_2 = \lambda_1^2\lambda_2^2 - 1$ are strain invariants of the principal stretches λ_1 and λ_2. The magnitude of the energy is ruled by the shear modulus E_s and the dilation modulus E_d. For the 2D case, one can derive a tension T given by [16]:

$$T = \frac{E_S}{2}\lambda_1(\lambda_1^2 - 1)\left(\frac{1 + C\lambda_1^4}{1 + C\lambda_1^2}\right)^{1/2}\left(1 + \frac{C(1 + C\lambda_1^2)}{(1 + C\lambda_1^4)^2}\right), \tag{35}$$

with $C = E_d/E_s \geq 10^4$ for a normal RBC. Next to the in-plane stresses, the bending rigidity E_b also plays a significant role for the dynamics of the RBC. Indeed, a bending stiffness which is too low will result in an easy deviation from the biconcave shape, which is optimal for the RBC's oxygen exchange capacity. On the other hand, a too high bending stiffness will restrict its motility in small capillaries, causing illness of the organism (as in the case of e.g. malaria). The bending moment M can be characterized by a linear formulation

$$M = E_b(\zeta - \zeta_0) \tag{36}$$

where ζ and ζ_0 are the actual and rest local curvatures. Having identified these forces, we only need to add T to each pair of particles in order to obtain the discrete in-plane interactions. For the bending forces, which act on a triplet of neighboring particles, we use a discretization according to which each outer particle with index $1, 3$ gets a force

$$F_{1,3} = \frac{E_b}{a^2}(\theta - \theta_0) \tag{37}$$

where a is the distance between the outer particle and the central particle, and θ is the angle of the triplet (see Fig. 8, right). In order to conserve the total momentum, a force $F_2 = -(F_1 + F_3)$ is exerted on the middle particle. Since a RBC has very little internal cytoskeletal structure, the viscoelastic behavior is dominated by the cortex and the cytoplasm behavior is assumed to be purely fluid-like.

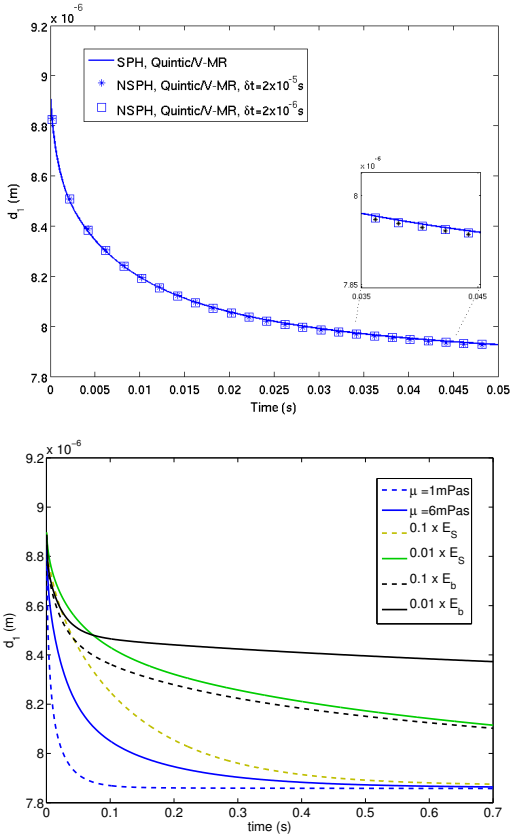

Figure 12: (Top) Simulated evolution of the radius d_1 during relaxation of the RBC. The relaxation curves obtained with SPH and NSPH are compared for the different viscous models (using $\mu = 1\,\mathrm{mPa}\cdot\mathrm{s}$) and time-steps. (Bottom) Parameter study of the NSPH model using a different elastic moduli E_b, E_S and viscosity.

We perform the *in silico* relaxation experiment by considering an initial undeformed RBC immersed in a fluid. The system is discretized with a particle resolution of $0.17\,\mu$m ($h = 0.147\,\mu$m), sufficient for a RBC with radius $3.9\,\mu$m. This results in 100 RBC membrane particles, with a total of 10000 fluid particles (plasma + cytoplasma) in our simulation. The elastic moduli are $E_s = 5 \times 10^{-6}\,\mathrm{N/m}$, $E_d = 0.1\,\mathrm{N/m}$, and $E_b = 2 \times 10^{-19}\,\mathrm{Nm}$ [16]. Both the cytoplasm and the suspending fluid viscosities are arbitrarily set to $\mu = 1 \times 10^{-3}\,\mathrm{Pa}\cdot\mathrm{s}$. The viscosity between the membrane particles is arbitrarily set to a slightly higher

value ($\mu = 1\times10^{-2}\,\mathrm{Pa}\cdot\mathrm{s}$) to account for the additional viscous forces originating in the lipid bilayer. The fluid particles are positioned in a periodic box on a square lattice, but some positions are replaced by the membrane particles' coordinates as given by Eq. (33). In order to avoid the non-uniform inter-particle distances that arise from this replacement, we initially run an equilibration simulation to smooth out these gaps. This can be done by recomputing the density of the particles by

$$\rho_i = \sum_j m_i W_{ij}. \tag{38}$$

If the particles are equally assigned with an initial density, particles in areas with under-sampling (gaps) will get a lower density, whereas particles with oversampling get higher densities. This will result in a penalization force originating from the EOS. As a result, a more uniform particle distribution will be obtained after a number of time-steps. After the equilibration, we stretch the cell by 15 % by pulling at the particles lying on the long axis of the cell in opposite directions. This results in a slight flattening out of the cell (see Fig. 11). Similar to the experiments performed in [32], we release the RBC and monitor the long axis diameter d_1 of the cell. Fig. 12 (top) depicts the relaxation evolution obtained with NSPH and standard SPH simulations (quintic/V-MR), showing a very good mutual agreement. It also shows that a time-step of $2 \times 10^{-5}\,\mathrm{s}$, restricted by the bending stiffness of the membrane, is sufficiently small[4].

We have also run simulations to better assess the influence of parameter variations on the relaxation time. Increasing the plasma viscosity to $6 \times 10^{-3}\,\mathrm{Pa}\cdot\mathrm{s}$ (the normal value in blood) results in an increased relaxation time from $\sim 0.03\,\mathrm{s}$ to $\sim 0.1\,\mathrm{s}$, the latter being in reasonably good agreement with experimental values of 0.1 s to 0.3 s [31, 35]. In addition to this, the effect of 10 times and 100 times lower elastic moduli is also given, indicating that the effect of bending on relaxation is larger compared to the membrane Young's modulus.

Finally, we look at the computational time that is required to run these simulations. For the SPH case with $\mu = 10^{-3}\,\mathrm{Pa}\cdot\mathrm{s}$, the time-step is restricted by Eq. (6) and set to $2.5 \times 10^{-9}\,\mathrm{s}$, thus totaling 8×10^7 integration steps to bridge a realistic time. In this example, the NSPH simulations need only 10^4 steps[5]. Running the complete simulations, we find that the NSPH runs are approximately 4000 times faster for this example.

4.6. Motion of a RBC in Poiseuille flow

The motion of RBC's in Poiseuille flow is very similar to blood flow in capillaries. Therefore, it is frequently used as a model case to show how RBCs need to deform to pass through capillaries smaller than their diameter. The system consists of two parallel plates (at a distance of $9.5\,\mu\mathrm{m}$) between which

[4] If the spring-bending connections are solved as a second order system, the required time-step is $2 \times 10^{-7}\,\mathrm{s}$.

[5] The convergence time to find the velocities in CGM can vary significanlty during the simulations.

the RBC is initially positioned in vertical direction. The length of the plates is $30\,\mu$m but periodic boundary conditions are imposed in the x direction (see Fig. 13). The system is represented by 12000 particles.

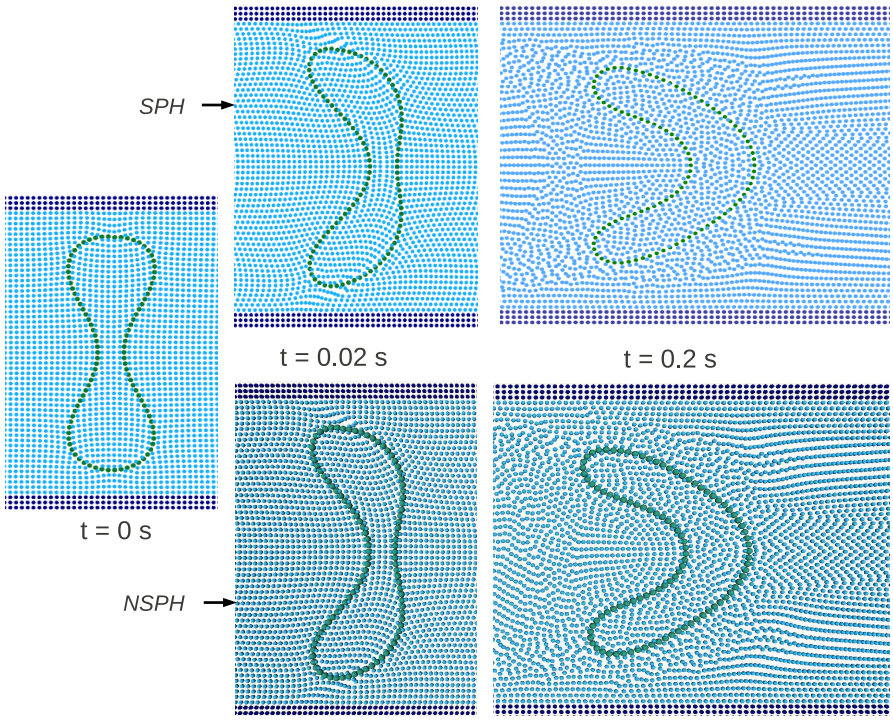

Figure 13: Snapshots of RBC configurations in Poiseuille flow for SPH (top) and NSPH (bottom) at different timepoints.

The same model parameters are used as in the previous section (with $\kappa = 10\,\mathrm{Pa}$), yet the fluid viscosity is set to $5 \times 10^{-3}\,\mathrm{Pa \cdot s}$. The particles are driven by a body force of $60\,\mathrm{N/m^2}$ and the flow has a realistic Reynolds number of 10^{-4}. The results of this simulation are depicted in Fig. 13. The parabolic velocity field causes the center of the cell to bulge forward and the cell evolves relatively quickly from a biconcave shape to a parachute shape ($t = 0.05\,\mathrm{s}$) and eventually arrives at a steady state, where the parachute has become smaller and slightly widened in the middle ($t = 0.1\,\mathrm{s}$, $t = 0.2\,\mathrm{s}$). Again, we compare the NSPH solution with the SPH results, which serve as the reference solution. Fig. 13 shows the evolution of the RBC shape in the flow at the beginning and after a longer time, while Fig. 14 shows the difference between the two models for the selected times. As can be observed, the shapes obtained with NSPH are in quite good agreement with those obtained from SPH. Additionally, the fluid

particle positions show very similar patterns while their velocity profiles match quite well for both methods.

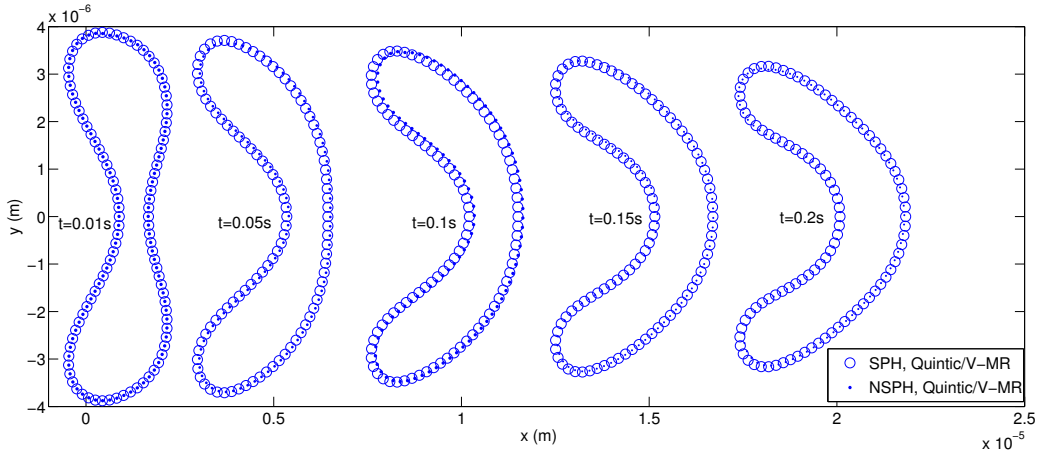

Figure 14: Comparison of shape and position of RBC for SPH and NSPH.

The attained speed-up in this example is roughly 2000 times, which is lower than in the previous example and probably due to the implementation of the periodic boundary conditions[6].

5. Conclusions and outlook

In this paper, we have proposed an alternative solution scheme to solve the Stokes equations, based on a meshfree particle approach. Starting from the standard SPH equations we have explicitly dropped the inertia term and solved the system as a set of linear equations, and this solution method is now further termed as NSPH. By a number of benchmarks, we have shown that NSPH reproduces results of the SPH model (after the initial transient behavior) quite well. While in the Poiseuille flow and Couette flow, the "correct" steady state velocity profiles are obtained after a single step for NSPH, more complicated systems as the shear driven cavity and the flow past cylinders actually require a few time-steps to converge, and a tuning of the balance between incompressibility and viscosity may be necessary. The long-term behavior of the NSPH simulations reveals that some numerical diffusion is present, in particular showing up in a decreasing magnitude of the velocity profiles for the viscous flow past an array of cylinders. However, these effects seem to be comparable with the regular SPH results, even if the particle configuration has become distorted.

[6]The time-step needed in SPH is smaller than 10^{-9} s.

In this regard, we also found that the choice of the interpolating kernel is very important in NSPH, and advice to use a quintic kernel.

To apply our model to microscopic biological systems, we have considered the transient relaxation behavior of a red blood cell and its motion in a capillary. The results from the NSPH simulations are in good agreement with the standard SPH solutions hereof. While the NSPH method can only be applied in low Reynolds systems, the big advantage is that potentially a much higher time-step ($\succ 1000\times$) can be used compared to SPH. While the SPH stability particularly suffers from a linear dependence of viscosity, and a quadratic dependence on the smoothing length, the NSPH stability depends on the balance of incompressibility and viscosity and is independent of the smoothing length. As such, we argue that NSPH could be a valuable alternative in microscopic (biological) systems which need to be modeled at a high spatio-temporal resolution, but where the long term time dependent behavior is of interest as well.

Finally, we want to mention that the Conjugate Gradient Method can be efficiently parallelized – as shown by e.g. Meurant [36]. For the present work, though, calculations on a single core were sufficiently quick, so that the additional implementation could be avoided. In a molecular dynamics software package that uses for example MPI for parallel communication and spatial domain decomposition, the CGM calculations can be distributed in the sub-domains that contain the information of the real particles and ghost particles.

6. Acknowledgements

This research is conducted utilizing high performance computational resources provided by the University of Leuven, http://ludit.kuleuven.be/hpc. The authors would like to thank Onderzoekstoelage (OT, KULeuven) and the Research Foundation - Flanders (FWO-Vlaanderen) for financial support. The authors are also grateful to Christian Hammann, Florian Johann and Tobias Seifen for the discussions about the Conjugate Gradient Method.

Appendix A. Proof that the CGM friction matrix is positive definite

We start by constructing the friction matrix Γ for N particles:

Γ is symmetrical by design, because the friction coefficient between two particles i and j is symmetric for a symmetric kernel W_{ij} Eq. (25):

$$\Gamma = \sum_{innj} \underbrace{\begin{pmatrix} 0 & \cdots & & & \\ \cdots & m_{ii} & \cdots & -m_{ij} & \cdots \\ \vdots & & \ddots & & \cdots \\ \cdots & -m_{ji} & \cdots & m_{jj} & \cdots \end{pmatrix}}_{M_{ij}} + \underbrace{\begin{pmatrix} d_{11} & 0 & & \cdots \\ 0 & d_{22} & 0 & \cdots \\ \vdots & & \ddots & \\ 0 & \cdots & & d_{NN} \end{pmatrix}}_{D}$$

where the sum runs over all pairs of interacting ("next-neighbor") particles and the elements $d_{ii} = \Gamma_{iw}$ and m are 2×2 matrices for a 2D system.

- The elements of D are diagonal matrices Γ_{iw} and contain values $\in \mathbb{R}^+$. Those can be used to "fix" the boundary particles in space by assigning very large values and therefore an "infinite" viscosity. For the fluid particles, we need to assign an arbitrarily small additional viscosity to ensure that the matrix is positive definite - see the last conclusion.

- The matrices m describe the interaction of two particles, and are defined in the following way:
  m is constructed as $m = \underbrace{\gamma_{\parallel} \boldsymbol{e}\boldsymbol{e}_{\boldsymbol{ij}}{}^t}_{a} + \underbrace{\gamma_{\perp}\left(I - \boldsymbol{e}_{\boldsymbol{ij}}\boldsymbol{e}_{\boldsymbol{ij}}{}^t\right)}_{b}$ where $\boldsymbol{e_{ij}}$ is the normalized direction vector between two particles and $\gamma_{\parallel}, \gamma_{\perp} \in \mathbb{R}^+$ are, respectively, the parallel and perpendicular friction constants. For the viscosity model V-MG, Eq. (19), $\gamma_{\perp}$ is zero, so the second part (b) of the sum can be disregarded.

- For m to be positive-definite, we need to show that $\boldsymbol{x}^t m \boldsymbol{x} > 0 \; \forall \boldsymbol{x} \in \mathbb{R}^2_{\setminus \mathbf{0}}$.

- Look at both parts of the sum:

  a: $\gamma_{\parallel} \boldsymbol{x}^t \boldsymbol{e_{ij}} \boldsymbol{e_{ij}}{}^t \boldsymbol{x} = \gamma_{\parallel} \left(\boldsymbol{x} \cdot \boldsymbol{e_{ij}}\right)^2 > 0$, so a is positive definite.

  b: $\gamma_{\perp}(\boldsymbol{x}^t \boldsymbol{x} - \boldsymbol{x}^t \boldsymbol{e_{ij}} \boldsymbol{e_{ij}}{}^t \boldsymbol{x}) \geq 0$:

  - True, iff $(\boldsymbol{x} \cdot \boldsymbol{x}) \geq \left(\boldsymbol{x} \cdot \boldsymbol{e_{ij}}\right)^2$
  - Using the Cauchy-Schwarz inequality: $\left(\boldsymbol{x} \cdot \boldsymbol{e_{ij}}\right)^2 \leq (\boldsymbol{x} \cdot \boldsymbol{x}) \cdot (\boldsymbol{e_{ij}} \cdot \boldsymbol{e_{ij}}) = (\boldsymbol{x} \cdot \boldsymbol{x}) \cdot 1$.

  $\Rightarrow$ b is positive semi-definite.

$\Rightarrow$ m is positive definite, since the sum of a positive definite matrix and a positive semi-definite matrix is positive definite.

- It remains to be proven that M_{ij} is positive semi-definite:
  Let us consider the two-particle case: $M_{ij} = \begin{pmatrix} m & -m \\ -m & m \end{pmatrix}$, since the generalization is obvious. We show that $\boldsymbol{x}^t M_{ij} \boldsymbol{x} \geq 0$:
  Let $\boldsymbol{x}^t = (\boldsymbol{a}, \boldsymbol{b})$ with $\boldsymbol{a}, \boldsymbol{b}$ chosen to be the basis of $\mathbb{R}^2$ for which m is diagonal with $m_{ii} \in \mathbb{R}^+$ - which is possible, since m is symmetrical and positive definite, as just proven, then:

$$\begin{aligned} \boldsymbol{x}^t M_{ij} \boldsymbol{x} &= \sum_{i=1}^{2} \left(a_i m_{ii} a_i + b_i m_{ii} b_i - a_i m_{ii} b_i - b_i m_{ii} a_i \right) \\ &= \sum_{i=1}^{2} m_{ii} \left(a_i - b_i \right)^2 \geq 0 \end{aligned}$$

$\Rightarrow$ M_{ij} is positive semi-definite, and since the sum of a positive semi-definite matrix and the positive-definite diagonal matrix D is positive definite,

$\Rightarrow$ Γ is positive definite. q.e.d.

Thanks to this result, in our algorithm, we solve the equation of motion Eq. (26) at each time-step as a coupled system for the velocities of the particles $\boldsymbol{v}$ with the Conjugate Gradient Method using the diagonal- or Jacobi-preconditioner, since the Matrix is diagonally dominated.

References

[1] L. Landau, E. Lifshitz, Fluid Mechanics, Pergamon Press, New York, 1959.

[2] C. Pozrikidis, Boundary Integral and Singularity Methods for Linearized Viscous Flow, Cambridge University Press, 1992.

[3] W. Hoover, Smooth particle applied mechanics: the state of the art, World Scientific Press, 2006.

[4] F. Jiang, M. Oliveira, A. Sousa, Comput. Phys. Commun. 176(7) (2007) 471–480.

[5] D. W. Holmes, J. R. Williams, P. Tilke, Int. J. Numer. Anal. Met. 35 (2011) 419–437.

[6] X. Hu, N. Adams, J. Comput. Phys. 213(2) (2006) 844–861.

[7] S. Nugent, H. Posch, Pys. Rev. E 62(4) (2000) 49684975.

[8] S. Adami, X. Hu., N. Adams, J. Comput. Phys. 229(5) (2010) 1909–1926.

[9] A. Tartakovsky, P. Meakin, Phys. Rev. E. 72(2) (2005).

[10] M. Ellero, R. Tanner, J. Non-Newtonian Fluid Mech. 132 (2005) 61–72.

[11] A. Rafiee, M. Manzari, M. Hosseini, Non-Linear Mechanics 42 (2007) 1210–1223.

[12] A. Vazquez-Quesada, M. Ellero, P. Espanol, J. Chem. Phys. 130 (2009) 034901.

[13] J. Monaghan, J. Comput. Phys. 159 (2000) 290–311.

[14] T. Jiang, J. Ouyang, J.-L. Ren, B.-X. Yang, X.-Y. Xu, Comput. Phys. Commun. 183 (2012) 50–62.

[15] J. Monaghan, Annual Review of Fluid Mechanics 44 (2012) 323–346.

[16] M. Hosseini, J. Feng, Chem. Eng. Sci. 64 (2009) 4488–4497.

[17] P. Van Liedekerke, E. Tijskens, H. Ramon, P. Ghysels, G. Samaey, D. Roose, Phys. Rev. E 81 (2010) 061906.

[18] P. V. Liedekerke, P. Ghysels, E. Tijskens, G. Samaey, D. Roose, H. Ramon, Soft Matter 7 (2011) 3580–3591.

[19] S. Sandersius, T. Newman, Physical Biology 5 (2008) 015002.

[20] C. B. Korn, U. S. Schwarz, Phys. Rev. E 77 (2008) 041904.

[21] J. Morris, P. Fox, Y. Zhu, J. Comput. Phys. 136 (1997) 214–226.

[22] S. Litvinov, M. Ellero, X. Hu, N. Adams, J. Comput. Phys. 229 (2010) 5457 – 5464.

[23] J. Monaghan, J. Comput. Phys. 138 (1997) 801–820.

[24] X.-J. Fan, R. Tanner, R. Zheng, J. Non-Newtonian Fluid Mech. 165 (2010) 219–226.

[25] W. Dehnen, H. Aly, Monthly Notices of the Royal Astronomical Society 425 (2012) 1068–1082.

[26] J. Monaghan, Rep. Prog. Phys. 68 (2005) 1703.

[27] J. Monaghan, J. Comput. Phys. 110 (1994) 399–406.

[28] M. T. Heath, Scientific Computing: An Introductory Survey, McGraw-Hill, 2nd edition, 2005.

[29] J. Monaghan, J. Kajtar, Comput. Phys. Commun. 180 (2009) 1811–1820.

[30] M. Ellero, N. A. Adams, Int. J. Numer. Meth. Eng. 86 (2011) 1027–1040.

[31] M. Dao, C. Lim, S. Suresh, Journal of the Mechanics and Physics of Solids 51(11) (2003) 2259–2280.

[32] F. Wottawah, S. Schinkinger, B. Lincoln, R. Ananthakrishnan, M. Romeyke, J. Guck, J. Kas, Phys. Rev. Lett. 94 (2005) 098103.

[33] I. Pivkin, G. Karniadakisa, Phys. Rev. Lett. 101 (2008) 118105.

[34] D. A. Fedosov, H. Lei, B. Caswell, S. Suresh, G. E. Karniadakis, PLoS Comput Biol 7 (2011) e1002270.

[35] P. Bronkhorst, G. Streekstra, J. Grimbergen, E. N. J. Sixma, G. Brakenhoff, Biophys J 95(5) (1995) 1666–1673.

[36] G. Meurant, Parallel Computing 5 (1987) 267 – 280.